Nanomechanical characterization of the deformation response of orthotropic Ti-6Al-4V

Carlos Rojas-Ulloa, Chantal Bouffioux, Andrés Jaramillo, Claudio M. García-Herrera, Tanvir Hussain, Laurent Duchêne, Guiomar Riu, Joan Josep Roa, Paulo Flores, Anne Marie Habraken, Víctor Tuninetti*

C. Rojas-Ulloa, Dr. A. Jaramillo, Prof. V. Tuninetti
Department of Mechanical Engineering, Universidad de La Frontera, Francisco Salazar 01145, Temuco 4780000, Chile
E-mail: victor.tuninetti@ufrontera.cl

Prof. C. M. García-Herrera
Departamento de Ingeniería Mecánica, Universidad de Santiago de Chile (USACH), Avenida Bernardo O'Higgins 3363, Santiago 9170022, Chile

C. Bouffioux, Prof. L. Duchêne, Dr. A. M. Habraken
ArGEnCo Department, MSM team, University of Liège, Quartier POLYTECH 1, allée de la Découverte 9, Liège 4000, Belgium

Prof. T. Hussain
Faculty of Engineering, University of Nottingham, Nottingham, NG7 2RD, UK

G. Riu, Prof. J. J. Roa
CIEFMA-Department of Materials Science and Engineering, Barcelona School of Engineering (EEBE), Universitat Politècnica de Catalunya-BarcelonaTech, Barcelona 08019, Spain

Prof. P. Flores
Department of Mechanical Engineering, Universidad de Concepción, Casilla 160 – C, Correo 3, Ciudad Universitaria, Concepción 4030000, Chile

Prof. J. J. Roa
Research Center in Multiscale Science and Engineering, Barcelona School of Engineering (EEBE), Universitat Politècnica de Catalunya-BarcelonaTech, Barcelona 08019, Spain

Dr. A. M. Habraken
Fonds de la Recherche Scientifique –F.R.S.– F.N.R.S., Belgium

Keywords: finite element modeling, nanoindentation, Berkovich, titanium alloys, tension-compression asymmetry, plastic anisotropy

The nanoindentation-induced mechanical deformation response is applied to identify the orthotropic elastic moduli using the Delafargue & Ulm method as well as to validate the asymmetric orthotropic

CPB06 non-linear plasticity model required in simulations of non-uniform macroscopic mechanical response of the Ti–6Al–4V alloy. Scanning electron microscope (SEM) technique allows to select the maximum penetration depth for the indentation in the deformed alpha phase and alpha-beta interphase; α- and α-/β-, respectively. The apparent macromechanical response could be successfully derived from several residual imprints conducted at micro- and/or submicrometric length scale and distributed throughout samples of the investigated bulk alloy, as demonstrated by correlation with finite element simulations based on the orthotropic elastoplastic model. The accurate numerical response obtained validates the material model and the Delafargue & Ulm approach, opening a window for next generation identification methods of macromechanical plasticity models with hybrid experimental-numerical method based on instrumented indentation and the use of SEM technique.

1. Introduction

The research interest in titanium alloys lies in the fact that their exceptional mechanical properties make them ideal for specific industrial applications, such as biomedical, aerospace and military industries.[1–3] Despite its high cost, Ti–6Al–4V alloy is currently the most widely used titanium alloy,[4] combining good biocompatibility and corrosion resistance,[5–10] high strength, low weight and ductility. [11–16]

Several manufacturing processes among the aforementioned applications contemplate the implementation of material characterization procedures, either on pristine samples of the material or on previously manufactured parts. The most commonly applied experimental procedures to identify the macroscopic orthotropic elastoplastic properties of a material include monotonic tensile,[17,18] compression[19,20] and shear[21,22] tests of material samples obtained from its orthogonal directions. The main limitations of these tests are the size of the specimens and their subsequent destruction, which characterize these types of testing as destructive. Although there are nondestructive techniques using the vibratory resonance response to characterize the elastic properties of samples, they do not allow direct identification of orthotropic properties. Some research studies have obtained orthotropic

constants by computing the vibration response using the finite element (FE) method or semi-analytical methods.[23–26] However, the knowledge of the dynamic response of Ti–6Al–4V provides directional and tension-compression asymmetrical elastic properties, as reported here and in previous studies.[13–16]

The rise of new technologies and manufacturing of highly critical components has brought a growing interest for non-destructive nanomechanical characterization procedures. Some applications requiring specific knowledge of nanomechanical behavior of these type of materials include BioMEMS,[27] porous implants,[28] and light weight micromechanical components.[29,30] Furthermore, correlation between the macroscopic and experimentally determined nanomechanical response for this and other alloys is substantially supported by recent research.[31–37] Hence, the aim of this research is to characterize the orthotropic elastoplastic response of Ti-6Al-4V at the nanometric length scales by applying a hybrid numerical-experimental method.

The instrumented indentation technique or depth-sensing nanoindentation technique, classified as a non-destructive method for characterizing the mechanical response of materials with the highest resolution,[38] allows load (P) and displacement (h) to be measured at the submicrometric length scale in order to determine the mechanical properties of the constitutive phases, as well as the micromechanical properties of the composite system. Standardized by ISO 14577-1, the depth range for nanoindentation is considered to maintain penetration distances below the sub-micrometric scale, with an average maximum depth of 2 μm.[39] This method allows to determine, in the direction of indentation, the elastic modulus of the tested sample from the unloading region in the loading-unloading (also known as loading-displacement or P-h) curve, while the surface hardness can be computed from the ratio between the maximum applied load (P_{max}) and the corresponding projected contact area (A_{pml}).[40,41] This method requires relatively small samples in comparison with other methods, and allows the mechanical properties of a wide range of materials to be obtained, from thick solid specimens to thin film coatings of metallic or polymer sheets.[35,40,42–48]

Indentation procedures have for long been used for determining the surface hardness of metallic materials. The acknowledging of an elastic behavior during the return of the indentation procedure led to the mathematical approach and further development of methods to obtain the elastic moduli of the indented material. Based on the solution of the classic contact problem through the Hertz approximation, and the J. R. Willis solution of the contact problem for anisotropic bodies through Fourier transforms,[49] Doerner & Nix[50] interpreted the unloading stage of a nanoindentation as an isotropic elastic contact problem between two bodies with different elastic constants. This method was lately improved by Oliver & Pharr[40]. Henceforth, in addition to the Vlassak & Nix[51] solution of the contact problem for two half-space surfaces by using Green function to describe the indenter surface, a solid framework was stablished for the development of a generalized method for identifying the elastic modulus and surface hardening of isotropic elastic materials through instrumented indentation tests at the nanometric length scale,[41,52] considering a wide range of indenter geometries (i.e. sharp and/or spherical tip indenters).

Although the Oliver & Pharr method[40] is widely used nowadays,[41–43,53–62] its application requires the elastic behavior of the indented material to be simplified, considering it as isotropic. Thus, for materials exhibiting orthotropic elasticity, the resultant elastic moduli are only an approximation. In view of this shortcoming, a mathematical approach for identifying the elastic moduli of materials exhibiting orthotropic elasticity from instrumented nanoindentation tests was developed by Delafargue & Ulm.[63] The mathematical framework for this method is based on the classical Hertzian contact problem throughout the simplification of the indenter tip as a rigid half-space surface through a Green function, describing the analytical relationship between load and indented area for isotropic materials.[64] Lately, Vlassak et al.[51] extrapolated the solution for materials exhibiting longitudinal and transversal anisotropy, and furthermore for generalized indenter geometries.[52] Based on the former approaches, Delafargue & Ulm[63] defined an analytical relation between the explicit elastic constants of an orthotropic material and the indentation induced mechanical response.

As shown in previous studies, this research topic continues to be of great interest for the engineering and scientific community.[34,36,48,55,65–67] A classical approach for studying the nanomechanical behavior of polycrystalline alloys is the nanoindentation modeling with crystal plasticity.[55,68–70] Other research studies inversely identify hardening properties such as hardening exponents by implementing artificial neural network.[53] In single crystals, the atomistic mechanisms of the anisotropic plasticity induced during nanoindentation tests are studied with molecular dynamics simulations.[57]

In this work, the methods proposed by Oliver & Pharr[40] and Delafargue & Ulm[63] were both applied for postprocessing the elastoplastic nanomechanical response of the α-/β- titanium alloy through numerical simulations of nanoindentation tests using the Lagamine FE software. The complex elastoplastic behavior of Ti–6Al–4V, exhibiting tensile-compressive asymmetry in plastic stresses, as well as distortional hardening,[12,14,15,55] is considered in further numerical FE simulations throughout the use of the CPB06 yield criterion,[71–73] acknowledging the reported distortional hardening phenomenon by including several asymmetric yield surfaces with different orthotropic material constants.[14,15] In conjunction with the classical Hooke's orthotropic law, this leads to high accuracy on the prediction of the mechanical deformation during nanoindentation. Firstly, microstructure identification was obtained with scanning electron microscopy (SEM) technique to select the maximum penetration depth of the indentation in order to deform the α-phase and alpha-beta α-/β-interphase contained in the investigated alloy. Several residual imprints were conducted at different penetration depths from nano- to micromechanical length scale, in order to determine the mechanical properties for each constitutive phase as well as for the composite. They were homogeneously distributed throughout the studied samples of the bulk alloy, defining the apparent macromechanical behavior which was successfully correlated with the FE simulations. The accurate numerical response predicted by the orthotropic elastoplastic model validated the material parameters, and the Delafargue & Ulm method[63] allowed quantification of the uncertainty errors between orthotropic Young moduli identification methods.[74] Within this context, the presented work

opens opportunities for future inverse identification procedures of mechanical plasticity models at different length scales by combining instrumented nanoindentation with the SEM imaging technique.

2. CPB06 yield criterion

Large strains elastoplastic behavior of hexagonal closed packed (hcp) materials such as titanium alloys is complex. The consideration of an orthotropic material with asymmetry in axial tension-compression stresses leads to a non-symmetric yield surface evolution.[14,15,71,73,75] In order to macroscopically describe the orthotropic elasticity and asymmetric crystallographic plasticity of Ti–6Al–4V, the CPB06 yield criterion[71,72] is chosen.

The equivalent stress described by CPB06 yield criterion is computed as follows:

$$\sigma_{\mathrm{eq}} = [(|\Sigma_1| - k\Sigma_1)^a + (|\Sigma_2| - k\Sigma_2)^a + (|\Sigma_3| - k\Sigma_3)^a]^{\frac{1}{a}} \quad (1)$$

where a is the degree of homogeneity of the function, k is the asymmetry parameter (variation of which leads to tension and compression stress asymmetry), and Σ_i (with i=1,2,3) are the eigenvalues of the transformed deviatoric stress tensor, i.e.:

$$\mathbf{\Sigma} = \mathbf{L}:\mathbf{S} \quad (2)$$

where **S** is the deviatoric stress tensor and **L** is the 4th order tensor of orthotropic constants, which, represented in Voigt notation as:

$$\mathbf{L} = \begin{pmatrix} L_{11} & L_{12} & L_{13} & 0 & 0 & 0 \\ L_{12} & L_{22} & L_{23} & 0 & 0 & 0 \\ L_{13} & L_{23} & L_{33} & 0 & 0 & 0 \\ 0 & 0 & 0 & L_{44} & 0 & 0 \\ 0 & 0 & 0 & 0 & L_{55} & 0 \\ 0 & 0 & 0 & 0 & 0 & L_{66} \end{pmatrix} \quad (3)$$

From the equivalent stress formula shown in Equation 1 the effective stress is computed as follows:

$$\overline{\sigma} = \widetilde{m}\sigma_{eq} \quad (4)$$

where $\tilde{m}$ is a constant defined such that the equivalent stress (σ_{eq}) is reduced to the yield stress in the main Longitudinal Direction (LD) of the material. In this direction, is also defined the current yield stress of the material using the Voce isotropic hardening law.

$$\sigma_y(\bar{\epsilon}^p) = R_0 + R_S[1 - \exp(-C_R\bar{\epsilon}^p)] \quad (5)$$

where the parameters R_0, R_S and C_R are, respectively, the initial yield stress, the saturation coefficient, and the saturation rate, while $\bar{\epsilon}^p$ is the equivalent plastic strain.

By subtracting the effective yield stress σ_y from the effective stress ($\bar{\sigma}$) of the material, the actual CPB06 yield criterion is obtained $\Phi = \bar{\sigma} - \sigma_y$.

2.1. Material parameters for the CPB06 yield criterion

The CPB06 yield criterion was used for modeling the mechanical behavior of the studied Ti–6Al–4V. Two sets of CPB06 yield criterion parameters have been found using different identification techniques. In the present work, the numerical simulations of nanoindentation are executed using the two sets of previously identified parameters to understand the effect of the identification in the FE simulation results.

The parameter k defines the asymmetry between tension and compression stresses, but only within plastic deformations. Recent research[14,15] has shown that Ti–6Al–4V also exhibits different elastic moduli in tensile and compressive stresses as summarized in **Table 1**.

In order to consider this phenomenon, different compliance matrices were defined for tensile and compressive stresses. The general form of the orthotropic elastic compliance matrix is shown in Equation 6.

$$\mathbf{C^e} = \begin{pmatrix} \frac{1}{E_{11}} & \frac{-\nu_{12}}{E_{11}} & \frac{-\nu_{13}}{E_{11}} & 0 & 0 & 0 \\ \frac{-\nu_{12}}{E_{11}} & \frac{1}{E_{22}} & \frac{-\nu_{23}}{E_{22}} & 0 & 0 & 0 \\ \frac{-\nu_{13}}{E_{11}} & \frac{-\nu_{23}}{E_{22}} & \frac{1}{E_{33}} & 0 & 0 & 0 \\ 0 & 0 & 0 & \frac{1}{2G_{12}} & 0 & 0 \\ 0 & 0 & 0 & 0 & \frac{1}{2G_{13}} & 0 \\ 0 & 0 & 0 & 0 & 0 & \frac{1}{2G_{23}} \end{pmatrix} \quad (6)$$

The stress state of the material during the nanoindentation tests depends on the position of the analyzed element; however, the dominant stress state is compressive. Considering this fact, the elastic moduli used for this simulation were determined by compression tests.

To determine the R_0, R_S and C_R parameters of the Voce's hardening law (Equation 5), two experimental characterizations were made along the LD direction of the material. The first, presented in Ref.[14] considered a maximum logarithmic strain of 0.10 during the experimental tensile test. The second, presented in Ref.[15] considered a maximum logarithmic strain of 0.20. They are hereafter referred to as (IJP) and (MEC) parameters, respectively.

3. Materials and methods

3.1. Mechanical properties at the submicrometric length scale

Prior to the microstructural and micromechanical properties characterization, the sample surfaces were grinded and polished using SiC abrasive paper up to 1200 grit and subsequently polished with 1 μm grit size diamond paste to reveal the microstructure. The nanoindentation tests were carried out with the iNano nanoindenter (Nanomechanics Inc., a KLA-Tencor Company, Oak Ridge, TN, USA) equipped with a Berkovich diamond tip indenter. Prior to the indentation process, the indenter tip was carefully calibrated using a standard fused silica specimen. The indentation tests were performed under loading control mode at 50 ± (3×10^{-6}) mN of maximum applied load in two directions of the material (LD and Short Transverse Direction (ST) as shown in **Figure 1**. The distance between

indentation imprints was held constant and equal to 20 µm in order to avoid any overlapping effect.[67] For each direction, 16 imprints (4×4) in 5 different samples of the volumetric ingot are enough to represent the mechanical properties at the micrometric length scale, giving better understanding of the macroscopic behavior of the investigated alloy (see **Figure 2**). More information related to the micromechanical response of the investigated material under instrumented nanoindentation tests is available in Ref.[32].

3.2. Nanoindentation post-processing methods for mechanical characterization

The P-h curve resulting from an experimental instrumented or FE simulated nanoindentation is obtained in the form of a set of points describing the load (P) and axial displacement (h) at a user-defined period of time. While the loading stage of the P-h curve represents a mixed elastoplastic behavior, the elastic behavior is responsible for the unloading stage.[50] This combined indenter-specimen elastic response at the unloading stage of the P-h curve is ruled by the reduced elastic modulus E_r (also known as effective elasti modulus). Following the fundamental Hertz contact solution,[51] the reduced elastic modulus E_r can be expressed as a function of the initial unloading stiffness S and the projected contact area at maximum load A_{pml}:

$$E_r = \frac{S}{2\beta}\sqrt{\frac{\pi}{A_{pml}}} \tag{7}$$

where β is the geometry correction factor. For a Berkovich indenter geometry, β=1.034.[76]

3.2.1. Oliver & Pharr method for isotropic elasticity

Considering the unloading indentation process as an interaction of two elastically isotropic deformable solids, E_r can be expressed as a function of the elastic moduli and Poisson's ratios of both the indenter and the indented materials, as follows:

$$\frac{1}{E_r} = \frac{1-\nu^2}{E} + \frac{1-\nu_i^2}{E_i} \tag{8}$$

where E and ν are the elastic modulus and Poisson's ratio of the indented material, while E_i and ν_i are the elastic constants of the indenter.

The Oliver & Pharr[40] method is widely used to determine the elastic modulus of indented materials with relatively good results;[32,35,44,45,47,54,55,60,77,78] however, it simplifies the elastic behavior of the material, treating it as entirely isotropic which is not suitable for accurate characterization of orthotropic elastic materials.

3.2.2. Delafargue & Ulm method for orthotropic elasticity

Although the Delafargue & Ulm[63] method was conceived for conical indenters, the A_{pml} between conical and Berkovich indenter geometries are equivalent, considering an apex cone angle of 70.3°.[79,80] In order to apply this method, E_r is denoted hereafter as M_k, where k stands for the indentation direction (k=1,2,3) and is related to the orthotropic material directions. Analogous to Equation 7, M_k in the k direction is computed from the P-h curve data.

$$M_k^{\mathrm{V}} = \frac{S_k}{2\beta}\sqrt{\frac{\pi}{A_{pml,k}}} \tag{9}$$

where S_k and $A_{pml,k}$ are respectively the initial unloading stiffness and projected contact area at maximum applied load presented in Equation 7, while the superscript V stands for Vlassak approach.

Now, following the Delafargue & Ulm[63] approach, M_k^D is then calculated as a function of the components of the stiffness matrix of the indented material.[63,74] The stiffness matrix, calculated as the inverse of the orthotropic compliance matrix (Equation 6), is expressed in Voigt notation as follows:

$$inv(\mathbf{C^e}) = \mathbf{C} = \begin{pmatrix} C_{11} & C_{12} & C_{13} & 0 & 0 & 0 \\ C_{21} & C_{22} & C_{23} & 0 & 0 & 0 \\ C_{31} & C_{32} & C_{33} & 0 & 0 & 0 \\ 0 & 0 & 0 & C_{44} & 0 & 0 \\ 0 & 0 & 0 & 0 & C_{55} & 0 \\ 0 & 0 & 0 & 0 & 0 & C_{66} \end{pmatrix} \tag{10}$$

The stiffness matrix is symmetric, so that $C_{ij}=C_{ji}$. Then, for orthotropic materials, the tensor contains 9 different constants: C_{11}, C_{12}, C_{13}, C_{22}, C_{23}, C_{33}, C_{44}, C_{55} and C_{66}.

Then, the reduced elastic modulus for indentations along the three orthogonal directions of the investigated alloy, i.e., 1 (LD), 2 Transverse Direction (TD) and 3 (ST), are:

$$\begin{cases} M_1^D = \sqrt{M_{12}M_{13}} \\ M_2^D = \sqrt{M_{21}M_{23}} \\ M_3^D = \sqrt{M_{31}M_{32}} \end{cases} \quad (11)$$

where the constants M_{ij} are functions of the orthotropic stiffness matrix components.

$$M_{21} = 2\sqrt{\frac{C_{21}^2 - C_{12}^2}{C_{11}}\left(\frac{1}{C_{66}} + \frac{2}{C_{21}+C_{12}}\right)^{-1}} \quad ; \quad M_{12} = M_{21}\sqrt{\frac{C_{11}}{C_{22}}}$$

$$M_{31} = 2\sqrt{\frac{C_{31}^2 - C_{13}^2}{C_{11}}\left(\frac{1}{C_{55}} + \frac{2}{C_{31}+C_{13}}\right)^{-1}} \quad ; \quad M_{13} = M_{31}\sqrt{\frac{C_{11}}{C_{33}}} \quad (12)$$

$$M_{32} = 2\sqrt{\frac{C_{32}^2 - C_{23}^2}{C_{22}}\left(\frac{1}{C_{66}} + \frac{2}{C_{32}+C_{23}}\right)^{-1}} \quad ; \quad M_{23} = M_{32}\sqrt{\frac{C_{22}}{C_{33}}}$$

Although the stiffness matrix presented in Equation 10 is symmetric, while working in Voigt notation the application of this method implies the redefinition of the components C_{21}, C_{31} and C_{32} as follows:

$$\begin{cases} C_{21}^* = \sqrt{C_{11}C_{22}} \\ C_{31}^* = \sqrt{C_{11}C_{33}} \\ C_{32}^* = \sqrt{C_{22}C_{33}} \end{cases} \quad (13)$$

This method has proven to be very accurate in calculating the orthotropic elastic moduli of materials from monotonic instrumented nanoindentation techniques and for nanomechanical characterization of thin film coatings.[46,63] In this work, an algorithm initially proposed in Ref.[74] is applied in order to find the orthotropic elastic constants of the material. It consists of finding the three main independent elastic moduli of the material (E_{11}, E_{22} and E_{33}) and the Poisson's ratios, assuming that

the corresponding shear moduli (G_{44}, G_{55} and G_{66}) can be written as functions of the elastic coefficients mentioned above, i.e.:

$$\begin{cases} G_{12} = \frac{E_{11}}{2(1+\nu_{12})} \\ G_{13} = \frac{E_{33}}{2(1+\nu_{13})} \\ G_{23} = \frac{E_{22}}{2(1+\nu_{23})} \end{cases} \quad (14)$$

The reduced elastic modulus for each orthogonal direction of the material are obtained directly from the application of the Vlassak[51] method by solving Equation 9 for every unloading curve. Meanwhile, the orthogonal elastic moduli of the indented material are calculated by applying the Delafargue & Ulm[63] method presented in Equation 11. As the indenter is considered to be a rigid body, the reduced elastic moduli and the indented material's elastic moduli are considered to be equivalent for each orthogonal direction. The resultant equivalency is presented in Equation 15, where M_k^V and M_k^D are respectively the reduced elastic modulus in the k^{th} direction ($k = 1,2,3$) calculated by the Vlassak[51] and the Delafargue & Ulm[63] methods.

$$\begin{cases} \frac{S_1}{2\beta}\sqrt{\frac{\pi}{A_{pml,1}}} = M_1^V \equiv M_1^D = \sqrt{M_{12}M_{13}} \\ \frac{S_2}{2\beta}\sqrt{\frac{\pi}{A_{pml,2}}} = M_2^V \equiv M_2^D = \sqrt{M_{21}M_{23}} \\ \frac{S_3}{2\beta}\sqrt{\frac{\pi}{A_{pml,3}}} = M_3^V \equiv M_3^D = \sqrt{M_{31}M_{32}} \end{cases} \quad (15)$$

In order to solve the equation system presented in Equation 15, the values of the reduced elastic modulus computed by the Vlassak[51] method are written as functions of the elastic constants of the material, i.e.: $M_k^D = f_k(E_{ii}, \nu_{ij})$. Then the values of the elastic constants are adjusted using a non-linear regression method to minimize the root mean square percentile error (RMSPE) between the methods for calculating the reduced and material elastic moduli:

$$RMSPE = \sqrt{\frac{1}{3}\sum_{k=1}^{3}\left(\frac{f_k - M_k^V}{M_k^V} \times 100\right)^2} \quad (16)$$

4. Numerical Procedure

4.1. Mesh

FE modeling of the Berkovich indenter tip and the material sample was performed using the GMSH software,[81] and the subsequent FE simulation was executed in Lagamine, a research FE software.[82–84] In order to optimize the software computation time, a symmetry along the Z=0 plane is imposed on the geometries of the indenter and the material sample.

The dimensions of the modeled material specimen in the order of Cartesian directions (X, Y, Z) are 20 μm length, 20 μm width, and 10 μm height. To obtain accurate numerical results, a fine mesh was generated within the localized plastic deformation zone with elements of aspect ratio close to 1.

The geometry of the Berkovich indenter tip is known and standardized; however, various studies using SEM or Atomic Force Microscopy (AFM) imaging techniques have shown the presence of round edges, also known as tip defects.[79,85] This is considered to be the main source of uncertainty in nanoindentation tests.[85,86] By means of AFM, Zong et al.[79] measured 12 different tip and edge radii in diamond Berkovich indenters. Their results show that the average tip radius is 52.2 nm, while the average edge radius is 49.7 nm. For the sake of simplicity, the FE modelling of the Berkovich indenter tip carried out in this research considers a tip and edge fillet radius of ρ=50 nm . Because of this fillet radius, the values of the angles α and γ in the tip geometry presented in **Figure 3** are 65.35° and 76.9° respectively.

The Ti–6Al–4V specimen is meshed using volumetric elements with 8 nodes, one point of integration and 24 degrees of freedom (DOF). In order to achieve contact between the indenter and the titanium alloy, 2D contact elements[82] with 4 points of integration were added all over the contact surface. The contact was achieved by means of a Penalty algorithm Coulomb friction constitutive law.[84] The optimal values found for the contact pressure coefficient k_p and frictional stress coefficient k_t, necessary for achieving convergence in the FE simulations with the penalty algorithm of the contact

constitutive law, are k_p=k_t=3.7×10^7. A sensitivity analysis was performed subsequently to address the effect of the Coulomb friction coefficient μ on the modeling of frictional contact. This analysis showed a negligible effect of the friction coefficient on the maximum load reached, which is consistent with the available literature.[77,87,88] As a result, further FE simulations considered a Coulomb friction coefficient μ=0.08 according to previous experimental results.[89]

In these Berkovich depth-sensing indentation tests, the A_{pml} post processing error related to the tip and edge radius has less effect on the results than in other indenter geometries, such as Vickers or conical.[90] In the present work, with further consideration that the average fillet radius (50 nm) is approximately 7% of the maximum penetration depth, this error is considered to be negligible for the computation of A_{pml}. However, using an accurate model for the indenter geometry reduces the error of the local deformation field and the load predictions used for further comparison with the results obtained experimentally.

4.2. Boundary conditions

The boundary conditions of the indented specimen are displacement limitations along Cartesian directions, imposed on specific transverse planes. To simulate the instrumented nanoindentation test, a uniform monotonic displacement is imposed at a master node of the indenter geometry along the Y axis, until a maximum applied load of 50 mN is reached. The maximum penetration depth reached is around 7% of the total height of the modeled specimen, while the maximum penetration distance between both rigid and contact elements is around 50 nm.

4.3. Constitutive law parameters

The constitutive yield criterion selected for the volumetric elements composing the Ti–6Al–4V specimen is the CPB06,[71] while the current effective yield stress is computed with the Voce isotropic hardening law.

The evolution of the yield surface along large strains on an hcp material shows irregular behavior, not only in its shape, but along the orthogonal material directions. Mathematically, besides the

presence of the asymmetry parameter k and the orthotropic constants matrix, the CPB06 yield criterion implemented in the Lagamine FE software considers different yield surfaces at specific plastic work levels.[12,14–16] The resultant yield surface parameters are found by generating a linear interpolation between each plastic work level $\left(W_P^{(i)} < W_P^{(current)} < W_P^{(i+1)}\right)$ at each time step, where the plastic work is defined as a function dependent on the equivalent plastic strain, and is computed as follows:

$$W_P(\bar{\epsilon}^p) = \int \sigma_y(\bar{\epsilon}^p) d\bar{\epsilon}^p = (R_0 + R_s)\bar{\epsilon}^p - \frac{R_s}{C_r}[1 - \exp(-C_r\bar{\epsilon}^p)] \quad (17)$$

The orthotropic elastic constants for the elastic compliance matrix $\mathbf{C}^e$, and the components of the orthotropic constants tensor **L** describing the five yield surfaces at different plastic work levels, both in Voigt notation, are shown in **Table 2**.

The Voce isotropic hardening law coefficients, asymmetry parameters k for both (IJP)[14] and (MEC)[15] identifications and, in the case of k, for each of the defined yield surfaces are summarized in **Table 3**.

The simulations executed in this work are intended to retrieve results for identifying the orthotropic elastic constants of the material in its three orthogonal directions LD, TD and ST. These results depend on the parameters used to describe the elastoplastic behavior of the material; in order to compare the prediction capabilities of the two (IJP and MEC) sets of parameters shown in Tables 2 and 3, two simulations for each orthogonal direction of the material are executed, one for each set of parameters. The directions of the material according to the orthogonal Cartesian axes for each simulation are shown in **Figure 4**.

4.4. Sensitivity Analysis

In order to optimize the computational efficiency of further simulations, a mesh sensitivity analysis was executed initially. The variable chosen was the load at maximum penetration depth achieved in

the simulation (700 nm). Six different meshes were assessed, with increasing numbers of elements but conserving the proportion between the edges of the elements. From the results of the sensitivity analysis (**Figure 5**), it can be concluded that the mesh marked with * containing 25088 elements provides enough accuracy for the purpose of analyzing the prediction ability of both IJP and MEC sets of parameters, and the Oliver & Pharr[40] and Delafargue & Ulm[63] methods.

4.5. Prediction ability for IJP and MEC parameters.

Two sets of parameters for the CPB06 yield criterion were identified for predicting the elastoplastic behavior of Ti–6Al–4V. The first set of parameters (IJP) has been identified with pre-necking input data, while the MEC parameters are an extension of IJP, taking into account the deformation behavior of the alloy for post-necking true strain values of 20%.[15] In order to compare the actual prediction capabilities of both sets of parameters (IJP and MEC), and to verify the input data that can be identified from the elastoplastic behavior induced by instrumented nanoindentation, two simulations were executed along the direction 1 (LD) of the material. In **Figure 6**, the results of the simulated indentation loading stage are compared with the experimental results obtained from the instrumented nanoindentation tests in the same direction.

From these results, it is observed that the load response and absolute error at the beginning of the P-h curves is very similar for both IJP and MEC sets of parameters. However, for indentation depths beyond 150 nm, the prediction absolute error for the model obtained with the MEC set of parameters shows a more decreasing trend than the predictions of the model with the IJP set of parameters. As the penetration depth increases, so does the material strain, and therefore, a hardening law identified at high or post-necking strains is more suitable for predicting the stress states of the material. From this it is concluded that the MEC set of parameters gives a more accurate representation of the elastoplastic behavior of the material at large strains. Accordingly, the FE simulations executed hereafter will only consider the MEC set of parameters.

5. Numerical simulations results

5.1. Nanoindentation stress and strain states

The CPB06 yield criterion has proven to be adequate for describing the elastoplastic behavior of the Ti–6Al–4V alloy.[12,14–16] According to the analysis presented in Section 4.5, the numerical results obtained using MEC parameters are processed using the FE software LS-Prepost® (Livermore Software Technology Corporation, USA). The effective stress and equivalent plastic strain in the indented specimen at maximum depth computed with the optimum set of parameters (MEC) are presented in **Table 4**.

The reaction forces measured during the loading stage of an indentation test are mostly affected by the zones undergoing the highest stress states. By comparing the effective stresses and corresponding equivalent plastic strains for each direction summarized in Table 4, it is seen that the zone exhibiting plastic deformations (i.e., $\bar{\epsilon}^p > 0$) is in fact concentrating the highest stress states. In order to present a more accurate depiction of the ongoing stress states at maximum depth, the five most representative elements of the simulated specimen in the direction 1 (LD) were selected for analyzing the principal stresses along with their corresponding orthogonal vectors. This analysis is presented in **Figure 7**.

The maximum principal stress in absolute magnitude is σ_3, with its unitary vector pointing outwards from the indenter tip surface. Furthermore, the principal stresses in elements D and E are very similar, with a clear dominance of σ_3 and close values for σ_1 and σ_2. The equivalent stress value of element E is lower than that of element D due to diffusion of the stress in the indented material. Although the dominant principal stresses of the investigated alloy undergoing a Berkovich nanoindentation are in fact compressive, and fairly similar in magnitude among the five representative elements, there is a clear presence of compressive triaxial stress states.

5.2. Strain rate analysis

All the nanoindentation simulations were executed following the experimental method explained in Section 3.1, considering a loading time of 30 s and an approximate return time of 90 s. The parameters

of the Voce hardening law for describing the effective yield stress of Ti–6Al–4V in the direction LD were identified with a tensile test at a constant strain rate of 1×10^{-3} s^{-1}. As seen in **Figure 8a**, the resultant average strain rate is 3×10^{-2} s^{-1}. However, the strain rate field during the nanoindentation is not uniform (**Figure 8b**). Furthermore, the presence of high triaxiality in the indented specimen causes higher equivalent stress values compared to uniaxial loading. The difference between the strain rate selected for identifying the isotropic hardening law and that present in the nanoindentation simulation and experimental tests, produces small variations in the stresses and overall plastic material response.[12,13,16,91,92]

5.3. Orthogonal load-displacement curves

The P-h curves and respective fitted unloading stiffness curves, unloading stiffness slope (S), maximum depth (h_{max}), penetration depth (h_p) and projected area at maximum applied load (A_{pml}) for the three FE simulations are shown in **Table 5**. To adjust the initial unloading stiffness line, the slope of which is needed to determine the reduced elastic moduli, a linear fitting procedure was performed considering the first 4 points of the initial unloading stage of the P-h curve. The intersection of this linear fit with the P = 0 axis is equal to h_p.

5.4. Computation of orthotropic elastic moduli

The reduced elastic moduli are computed by solving Equation 7 for the three nanoindentation simulations, using the data presented in Table 5 and following the Vlassak & Nix[51] method. These results are presented in **Table 6**, and include the standard deviation of the CPB06 numerical model associated to the MEC set of parameters for the CPB06 yield criterion. The error associated to the load and shape prediction for this set of parameters are, respectively, 2.16% and 1.26%.[15] These results are used below to calculate the macroscopic Ti–6Al–4V elastic moduli using both the Oliver & Pharr[40] and Delafargue & Ulm[63] methods.

5.4.1. Isotropic approach

Due to the fact that only rigid elements were used to mesh the geometry of the Berkovich indenter tip, Equation 8 is now redefined as a function that depends only on the elastic constants of the indented material, where $E_{r,k}$ and E_k are respectively the relative and elastic modulus in the k^{th} orthogonal direction of the material (k=1,2,3), while v is the Poisson ratio.

$$\frac{1}{E_{r,k}} = \frac{1-\nu^2}{E_k} \quad \rightarrow \quad E_k = E_{r,k}(1-\nu^2) \tag{18}$$

Then, the three orthogonal elastic moduli of the material E_k are calculated using the Delafargue & Ulm[63] method by solving Equation 18.

5.4.2. Orthotropic approach

The application of the Delafargue & Ulm[63] method is reduced to the resolution of the equation system presented in Equation 15 through the optimization algorithm proposed in Equation 16, resulting in the computation of the orthogonal elastic constants of the material.

6. Results and discussion

The experimental compressive orthotropic elastic moduli of Ti–6Al–4V in conjunction with the obtained orthotropic elastic moduli calculated using the isotropic Oliver & Pharr[40] and the orthotropic Delafargue & Ulm[63] methods, including their respective standard deviations, are presented in **Table 7.** A posterior analysis of these results show that the average associated relative error for the Oliver & Pharr[40] method is of 20.8%, while for the Delafargue & Ulm method it is of -3.7%. This shows a significant improvement in the calculation of the orthotropic elastic moduli of the material. Nevertheless, in order to demonstrate this fact and the actual capabilities of the Delafargue & Ulm[63] method, it is mandatory to perform a more extensive experimental campaign, considering a wide range of materials exhibiting orthotropic elasticity, enabling the execution of a conclusive statistical analysis, such as ANOVA.

The CPB06[71] yield criterion has proven to be accurate for modeling the nanomechanical behavior of this material. However, in order to perform cyclic loading simulations and acknowledge the observed creep during nanoindentations,[32] it is mandatory to use more complex models, considering hardening and fatigue hardening components.[93]

7. Conclusions

The elastoplastic mechanical behavior of Ti–6Al–4V bulk specimen at micro- and submicrometric length scales exhibits orthotropic elasticity, distortional hardening and tension-compression stress asymmetry in plastic stress states. Accurate mechanical prediction of Ti–6Al–4V behavior along large strains is achieved using the CPB06 yield criterion in conjunction with an improved set of parameters, obtaining a negligible difference between numerical and experimental P-h curves during nanoindentation FE simulations. The effective stress and equivalent plastic strain scalar field show high magnitudes along the imprint zone. Subsequent tensorial analysis of the principal stresses across the indentation zone shows the presence of high-magnitude triaxial compressive stresses. Combined with the fact that the Ti–6Al–4V alloy has proven to exhibit asymmetry in tension-compression elastic moduli and plastic stress states, this demonstrates that simplification of the material as isotropic and symmetric has a detrimental impact on the indentation analysis and further computation of material constants. In this sense, in order to be able to conduct accurate nanoindentation FE simulations it is mandatory to characterize the material considering a variety of phenomena, such as: orthotropy, asymmetry, and hardening at large deformations; as well as considering an adequate plasticity model such as CPB06, which is capable of predicting these phenomena.

The use of Delafargue & Ulm method for determining the orthotropic elastic constants of materials exhibiting orthotropic elasticity through post-processing of nanoindentation P-h curves has proven to be far more accurate in comparison with the Oliver & Pharr method. This reveals that the isotropic simplification of the elastic behavior of the material along with the use of Oliver & Pharr method

does not retrieve reliable results when materials exhibit orthotropic elasticity and triaxial stress states during nanoindentation tests.

Acknowledgements
This work was funded by the National Agency for Research and Development (ANID) Fondecyt 11170002 and the cooperation agreement WBI/AGCID SUB2019/419031 (DIE19-0005). As research director of FRS-FNRS, A.M. Habraken thanks the Belgian Scientific Research Fund FNRS for financial support; and J.J. Roa acknowledges the Serra Hunter programme from the Generalitat de Catalunya. The authors also acknowledge the Dirección de Investigación (Universidad de La Frontera) for partial funding, Fondequip EQM170220 and FONDEQUIP EQM130014.

Received: ((will be filled in by the editorial staff))
Revised: ((will be filled in by the editorial staff))
Published online: ((will be filled in by the editorial staff))

References

[1] M. Legros, A. Couret, D. Caillard, *J. Mater. Sci.* **2006**, *41*, 2647.

[2] L.-C. Zhang, L.-Y. Chen, L. Wang, *Adv. Eng. Mater.* **2020**, *22*, 1901258.

[3] L. Kang, C. Yang, *Adv. Eng. Mater.* **2019**, *21*, 1801359.

[4] J. C. Williams, R. R. Boyer, *Metals (Basel).* **2020**, *10*, 705.

[5] H. Hassanin, F. Modica, M. A. El-Sayed, J. Liu, K. Essa, *Adv. Eng. Mater.* **2016**, *18*, 1544.

[6] D. Faria, C. S. Abreu, M. Buciumeanu, N. Dourado, O. Carvalho, F. S. Silva, G. Miranda, *J. Biomed. Mater. Res. - Part B Appl. Biomater.* **2018**, *106*, 1534.

[7] L. Zhang, L. Chen, *Adv. Eng. Mater.* **2019**, *21*, 1801215.

[8] D. Cáceres, C. Munuera, C. Ocal, J. A. Jiménez, A. Gutiérrez, M. F. López, *Acta Biomater.* **2008**, *4*, 1545.

[9] N. Dai, L.-C. Zhang, J. Zhang, X. Zhang, Q. Ni, Y. Chen, M. Wu, C. Yang, *Corros. Sci.* **2016**, *111*, 703.

[10] I. Campioni, N. Gupta, *Med. DEVICES SENSORS* **2020**, 1.

[11] V. Tuninetti, G. Gilles, O. Milis, L. Lecarme, A.-M. Habraken, *Steel Res. Int.* **2012**, *S.E.: 14th Int. Conf. Metal Forming 2012 in Ref 11*, 1239.

[12] V. Tuninetti, A. M. Habraken, *Mater. Sci. Eng. A* **2014**, *605*, 39.

[13] C. F. Guzmán, V. Tuninetti, G. Gilles, A. M. Habraken, *Key Eng. Mater.* **2015**, *651–653*, 575.

[14] V. Tuninetti, G. Gilles, O. Milis, T. Pardoen, A. M. Habraken, *Int. J. Plast.* **2015**, *67*, 53.

[15] V. Tuninetti, G. Gilles, P. Flores, G. Pincheira, L. Duchêne, A. M. Habraken, *Meccanica* **2019**, *54*, 1823.

[16] V. Tuninetti, P. Flores, M. Valenzuela, G. Pincheira, C. Medina, L. Duchêne, A.-M. Habraken, *Int. J. Mater. Form.* **2020**, DOI 10.1007/s12289-020-01543-2.

[17] S. Cecchel, D. Ferrario, G. Cornacchia, M. Gelfi, *Adv. Eng. Mater.* **2020**, *22*, 2000359.

[18] P. Flores, V. Tuninetti, G. Gilles, P. Gonry, L. Duchêne, A. M. Habraken, *J. Mater. Process. Technol.* **2010**, *210*, 1772.

[19] Z. Jia, X. Sun, J. Ji, Y. Wang, B. Wei, L. Yu, *Adv. Eng. Mater.* **2020**, DOI 10.1002/adem.202001048.

[20] C. Li, Z. Ding, S. van der Zwaag, *Adv. Eng. Mater.* **2021**, *23*, 1901552.

[21] A. Brosius, Q. Yin, A. Güner, A. E. Tekkaya, *steel Res. Int.* **2011**, *82*, 323.

[22] S. Li, C. Guo, L. Hao, Y. Kang, Y. An, *steel Res. Int.* **2019**, *90*, 1900311.

[23] m. dalaei, A. d. Kerr, *J. Sound Vib.* **1996**, *189*, 399.

[24] H. R. Javidrad, S. Salemi, *Int. J. Adv. Manuf. Technol.* **2020**, *107*, 4597.

[25] M. . Ahmadian, M. Sherafati Zangeneh, *Comput. Methods Appl. Mech. Eng.* **2002**, *191*, 2097.

[26] T. S. Koko, M. D. Olson, *J. Sound Vib.* **1992**, *158*, 149.

[27] M. Birkholz, K. E. Ehwald, P. Kulse, J. Drews, M. Fröhlich, U. Haak, M. Kaynak, E. Matthus, K. Schulz, D. Wolansky, *Adv. Funct. Mater.* **2011**, *21*, 1652.

[28] S. Liu, J. Liu, L. Wang, R. L.-W. Ma, Y. Zhong, W. Lu, L.-C. Zhang, *Scr. Mater.* **2020**, *181*, 121.

[29] T. N. Pornsin-Sirirak, Y. C. Tai, H. Nassef, C. M. Ho, *Sensors Actuators, A Phys.* **2001**, *89*, 95.

[30] M. Nasr Esfahani, B. E. Alaca, *Adv. Eng. Mater.* **2019**, *21*, 1900192.

[31] Z. Wu, S. Sandlöbes, J. Rao, J. S. K. L. Gibson, B. Berkels, S. Korte-Kerzel, *Mater. Des.* **2018**,

157, 337.

[32] V. Tuninetti, A. F. Jaramillo, G. Riu, C. Rojas-Ulloa, A. Znaidi, C. Medina, A. M. Mateo, J. J. Roa, *Metals (Basel).* **2021**, *11*, 104.

[33] I. Sen, S. Roy, M. F. X. Wagner, *Adv. Eng. Mater.* **2017**, *19*, DOI 10.1002/adem.201700298.

[34] Y. Wen, L. Xie, Z. Wang, L. Wang, W. Lu, L. C. Zhang, *J. Mater. Res. Technol.* **2019**, *8*, 3434.

[35] S. Guessasma, W. Zhang, J. Zhu, *J. Appl. Polym. Sci.* **2017**, *134*, 1.

[36] F. Han, B. I. N. Tang, X. U. Yan, Y. Peng, H. Kou, *Metall. Mater. Trans. A* **2017**, *48*, 2051.

[37] L. Wang, L. Xie, Y. Lv, L.-C. Zhang, L. Chen, Q. Meng, J. Qu, D. Zhang, W. Lu, *Acta Mater.* **2017**, *131*, 499.

[38] R. F. Cook, *Science (80-.).* **2010**, *328*, 183.

[39] *International Standard of Organization, ISO 14577-1: Metallic Materials — Instrumented Indentation Test for Hardness and Materials Parameters*, **2002**.

[40] W. C. Oliver, G. M. Pharr, *J. Mater. Res.* **1992**, *7*, 1564.

[41] W. C. Oliver, G. M. Pharr, *J. Mater. Res.* **2004**, *19*, 3.

[42] R. Saha, W. D. Nix, *Acta Mater.* **2002**, *50*, 23.

[43] M. Zhao, X. Chen, Y. Xiang, J. J. Vlassak, D. Lee, N. Ogasawara, N. Chiba, Y. X. Gan, *Acta Mater.* **2007**, *55*, 6260.

[44] A. Clausner, F. Richter, *Eur. J. Mech. - A/Solids* **2015**, *51*, 11.

[45] M. Fátima Vales Silva, P. Hancock, J. R. Nicholls, *Adv. Eng. Mater.* **2000**, *2*, 671.

[46] W. Y. Huen, H. Lee, V. Vimonsatit, P. Mendis, H.-S. Lee, *Sci. Rep.* **2020**, *10*, 11176.

[47] S. Sinha, R. A. Mirshams, T. Wang, S. S. Nene, M. Frank, K. Liu, R. S. Mishra, *Sci. Rep.* **2019**, *9*, 6639.

[48] J. H. Ahn, D. Kwon, *Mater. Sci. Eng. A* **2000**, *285*, 172.

[49] J. R. Willis, *J. Mech. Phys. Solids* **1966**, *14*, 163.

[50] W. D. Doerner, M. F., Nix, *J. Mater. Res.* **1986**, *1*, 601.

[51] J. J. Vlassak, W. D. Nix, *Philos. Mag. A Phys. Condens. Matter, Struct. Defects Mech. Prop.*

1993, *67*, 1045.

[52] J. J. Vlassak, M. Ciavarella, J. R. Barber, X. Wang, *J. Mech. Phys. Solids* **2003**, *51*, 1701.

[53] H. Lee, W. Y. Huen, V. Vimonsatit, P. Mendis, *Sci. Rep.* **2019**, *9*, 1.

[54] C. Schneider-maunoury, A. Albayda, O. Bartier, L. Weiss, G. Mauvoisin, X. Hernot, *Mater. Today Commun.* **2020**, *25*, 1.

[55] A. Tiwari, S. Natarajan, Eds. , *Applied Nanoindentation in Advanced Materials*, John Wiley & Sons, Ltd, Chichester, UK, **2017**.

[56] Y. G. Li, P. Kanouté, M. François, D. Chen, H. W. Wang, *Int. J. Solids Struct.* **2019**, *156–157*, 163.

[57] K. Nishimura, R. K. Kalia, A. Nakano, P. Vashishta, *Appl. Phys. Lett.* **2008**, *92*, 161904.

[58] P. B. F. Soares, S. A. Nunes, S. D. Franco, R. R. Pires, D. Zanetta-Barbosa, C. J. Soares, *Braz. Dent. J.* **2014**, *25*, 385.

[59] C. Chang, D. Verdi, M. A. Garrido, J. Ruiz-Hervias, *Bol. la Soc. Esp. Ceram. y Vidr.* **2016**, *55*, 136.

[60] E. Broitman, *Tribol. Lett.* **2017**, *65*, 1.

[61] J. Dean, J. M. Wheeler, T. W. Clyne, *Acta Mater.* **2010**, *58*, 3613.

[62] C. Guo, L. Hao, Y. Kang, S. Li, Y. An, *Mater. Res. Express* **2019**, *6*, 096585.

[63] A. Delafargue, F.-J. Ulm, *Int. J. Solids Struct.* **2004**, *41*, 7351.

[64] J. R. Barber, **1974**, 230.

[65] T. Jun, D. E. J. Armstrong, T. B. Britton, *J. Alloys Compd.* **2016**, *672*, 282.

[66] B. Wu, N. Vajragupta, J. Lian, U. Hangen, P. Wechsuwanmanee, S. Münstermann, *Mater. Des.* **2017**, *121*, 154.

[67] P. Sudharshan Phani, W. C. Oliver, *Mater. Des.* **2019**, *164*, 107563.

[68] F. Han, B. Tang, H. Kou, J. Li, Y. Feng, *Mater. Sci. Eng. A* **2015**, DOI 10.1016/j.msea.2014.11.090.

[69] M. Zhang, J. Li, B. Tang, H. Kou, J. Fan, *Prog. Nat. Sci. Mater. Int.* **2018**, 0.

[70] D. Raabe, *Adv. Mater.* **2002**, *14*, 639.

[71] O. Cazacu, B. Plunkett, F. Barlat, *Int. J. Plast.* **2006**, *22*, 1171.

[72] O. Cazacu, F. Barlat, in *Multiscale Model. Heterog. Mater.*, ISTE, London, UK, **2008**, pp. 71–89.

[73] Rym Harbaoui, Olfa Daghfas, Amna Znaidi, Victor Tuninetti, *Frat. ed Integrità Strutt.* **2020**, *14*, 295.

[74] C. Lamuta, *SN Appl. Sci.* **2019**, *1*, 1263.

[75] D. Banabic, F. Barlat, O. Cazacu, T. Kuwabara, *Int. J. Mater* **2020**, DOI 10.1007/s12289-020-01580-x.

[76] R. B. King, *Int. J. Solids Struct.* **1987**, *23*, 1657.

[77] T. H. Wang, T.-H. Fang, Y.-C. Lin, *Mater. Sci. Eng. A* **2007**, *447*, 244.

[78] X. Tang, A. El-Hami, K. El-Hami, M. Eid, C. Si, *Sci. Rep.* **2017**, *7*, 1.

[79] W. J. Zong, D. Wu, C. L. He, *Meas. J. Int. Meas. Confed.* **2017**, *104*, 243.

[80] A. C. Fischer-cripps, *Fracture Mechanics*, Springer Berlin Heidelberg, Berlin, Heidelberg, **2006**.

[81] C. Geuzaine, J.-F. Remacle, *Int. J. Numer. Methods Eng.* **2009**, *79*, 1309.

[82] R. Charlier, A. M. Habraken, *Comput. Geotech.* **1990**, *9*, 59.

[83] S. Cescotto, R. Charlier, *Int. J. Numer. Methods Eng.* **1993**, *36*, 1681.

[84] A. M. Habraken, S. Cescotto, *Math. Comput. Model.* **1998**, *28*, 153.

[85] J. Čech, P. Haušild, O. Kovářík, A. Materna, *Mater. Des.* **2016**, *109*, 347.

[86] N. Panich, P. Wangyao, S. Surinphong, Y. K. Tan, Y. Sun, L. Le, U. Kingdom, *J. Met. Mater. Miner.* **2007**, *17*, 43.

[87] P. Berke, F. El Houdaigui, T. J. Massart, *Wear* **2010**, *268*, 223.

[88] M. Khelifa, V. Fierro, A. Celzard, *J. Mech. Sci. Technol.* **2014**, *28*, 3209.

[89] H. H. Ding, V. Fridrici, J. Geringer, J. Fontaine, P. Kapsa, *Tribol. Int.* **2019**, *135*, 368.

[90] T. Y. Tsui, W. C. Oliver, G. M. Pharr, *Mater. Res. Soc. Symp. - Proc.* **1997**, *436101997*, 147.

[91] V. Tuninetti, S. Yuan, G. Gilles, C. F. Guzmán, A. M. Habraken, L. Duchêne, *J. Phys. Conf. Ser.* **2016**, *734*, 032075.

[92] X.-M. Chen, Y. C. Lin, H.-W. Hu, S.-C. Luo, X.-J. Zhou, Y. Huang, *Adv. Eng. Mater.* **2021**, *23*, 2000704.

[93] H. Morch, L. Duchêne, R. Harzallah, V. Tuninetti, A. M. Habraken, *Eur. J. Mech. A/Solids* **2021**, *85*, DOI 10.1016/j.euromechsol.2020.104116.

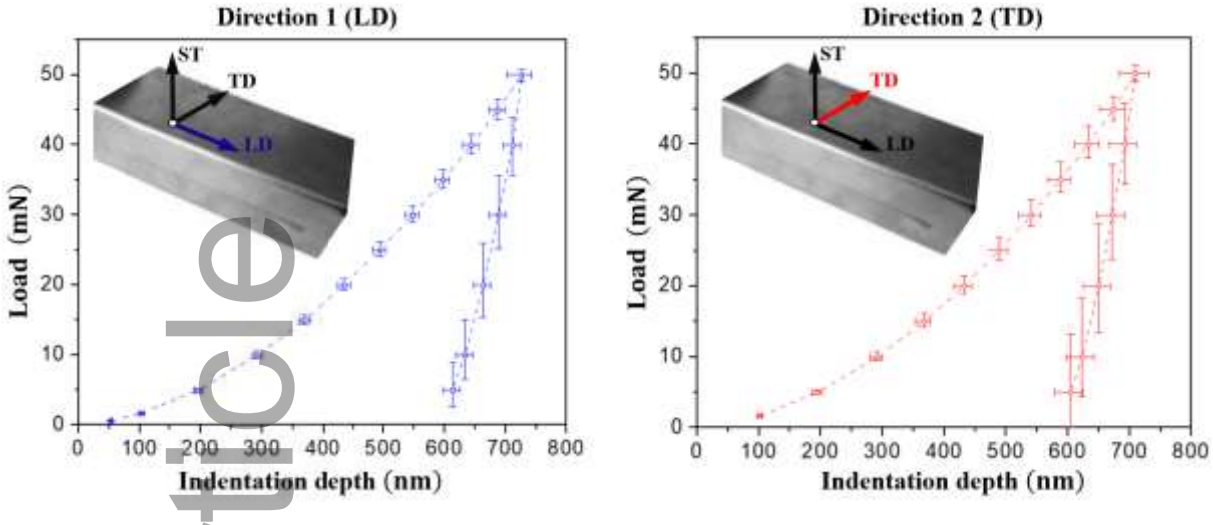

Figure 1: Average P-h curves from experimental nanoindentation tests on Ti–6Al–4V specimen in 1 (LD) and 2 (TD) directions.

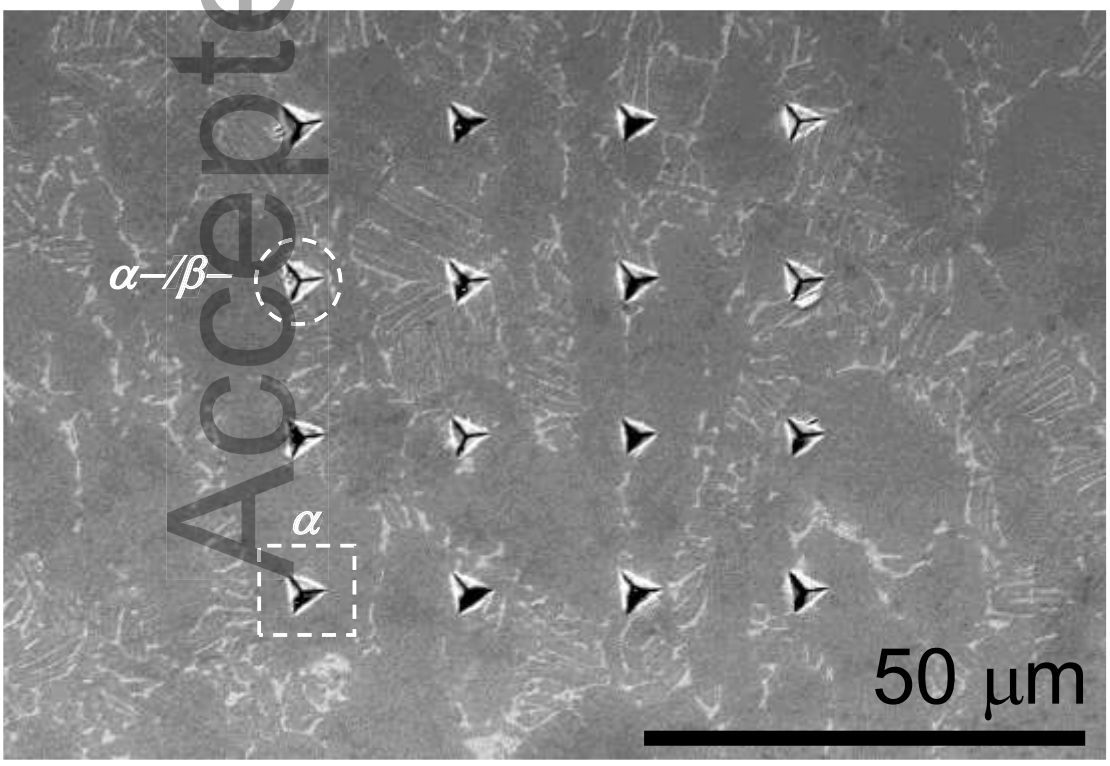

Figure 2. SEM micrograph of one array of imprints conducted at 700 nm of maximum penetration depth. Dashed circle shows a residual imprint performed at the α-/β-interphase and dashed square at the alpha phase.

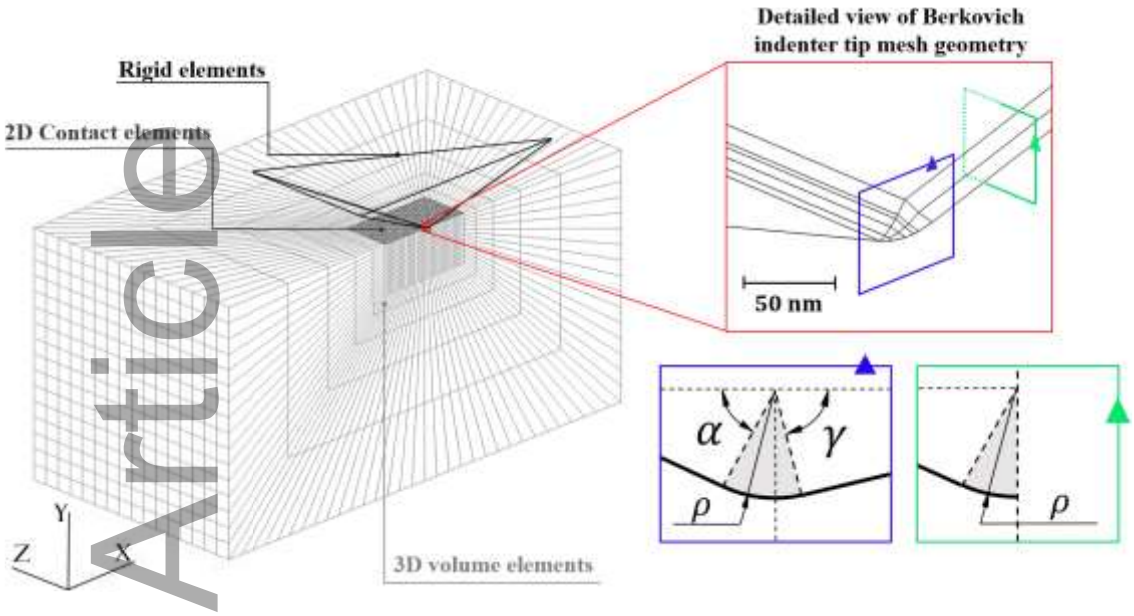

Figure 3. Berkovich indenter meshing and geometry specifications. The triangles are used for specifying the orientation of the view planes.

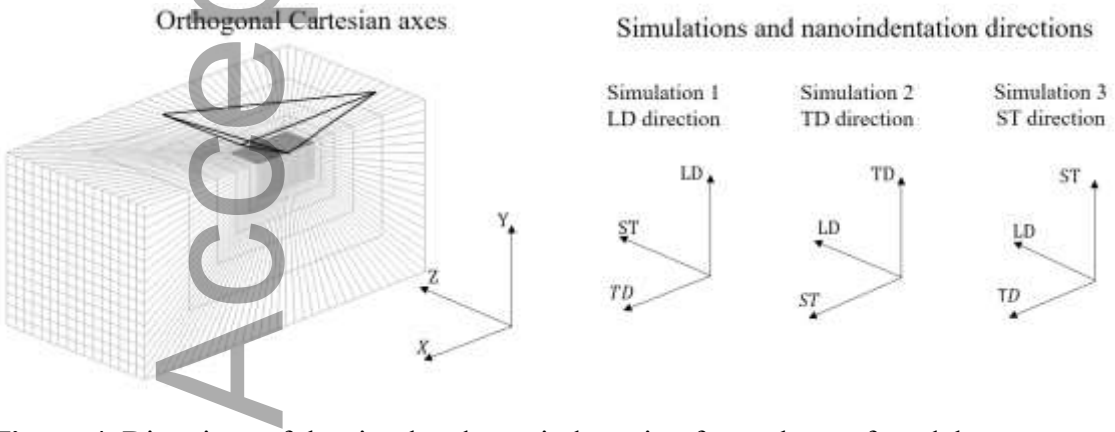

Figure 4. Directions of the simulated nanoindentation for each set of model parameters.

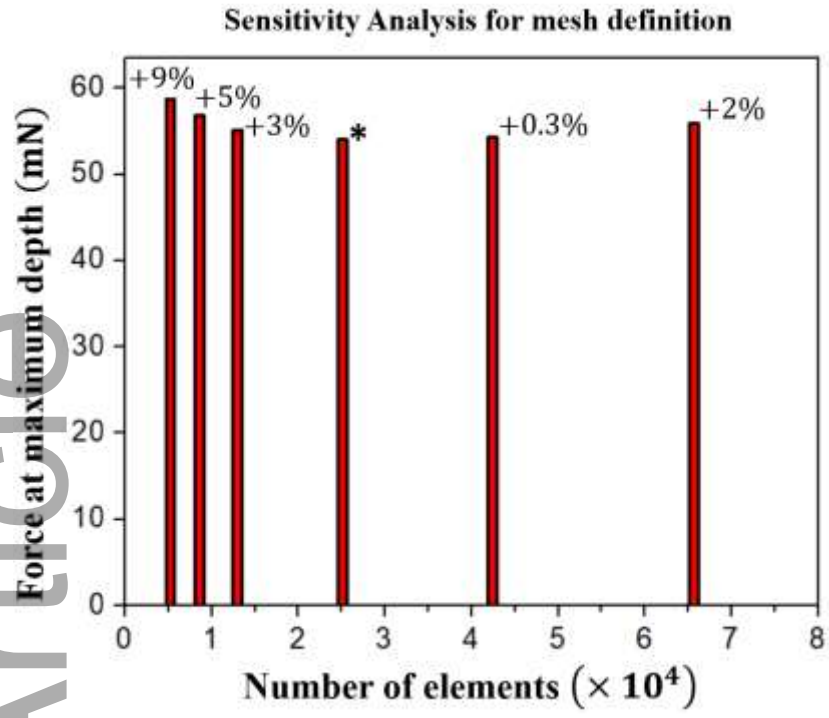

Figure 5. Sensitivity analysis results for the six different meshes.

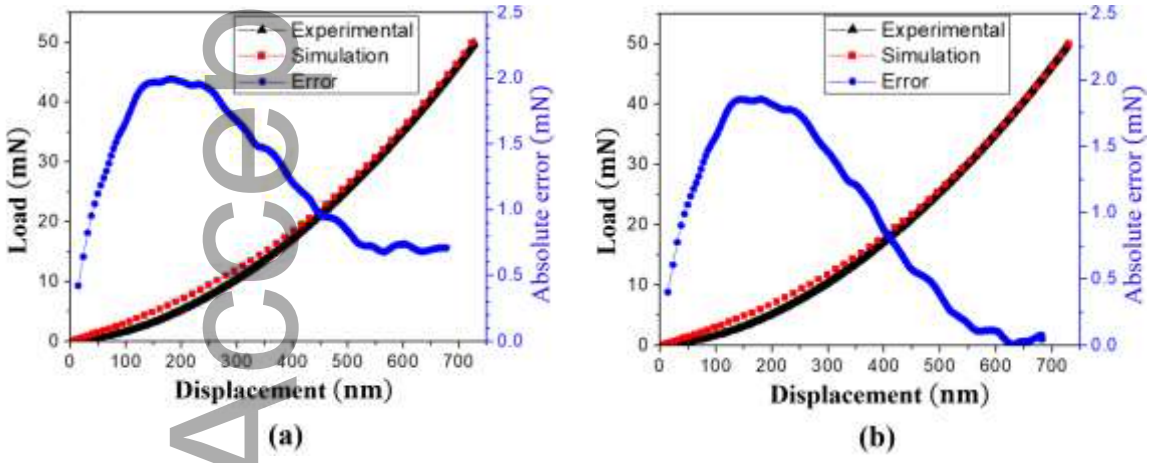

Figure 6. Comparison of experimental and numerical load-displacement curves for both IJP **(a)** and MEC **(b)** sets of parameters.

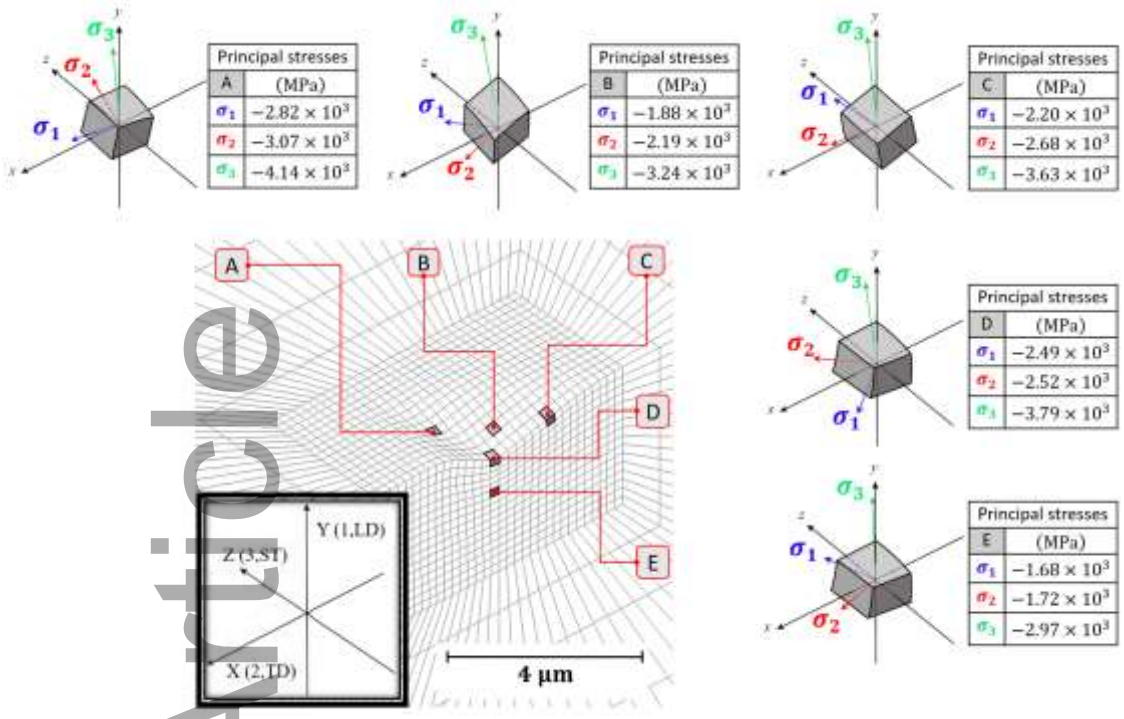

Figure 7. Principal stress states of Berkovich nanoindentation in Ti–6Al–4V alloy sample at maximum depth. It must be noted that every principal stress does have its counteracting part, accomplishing Newton 1st law.

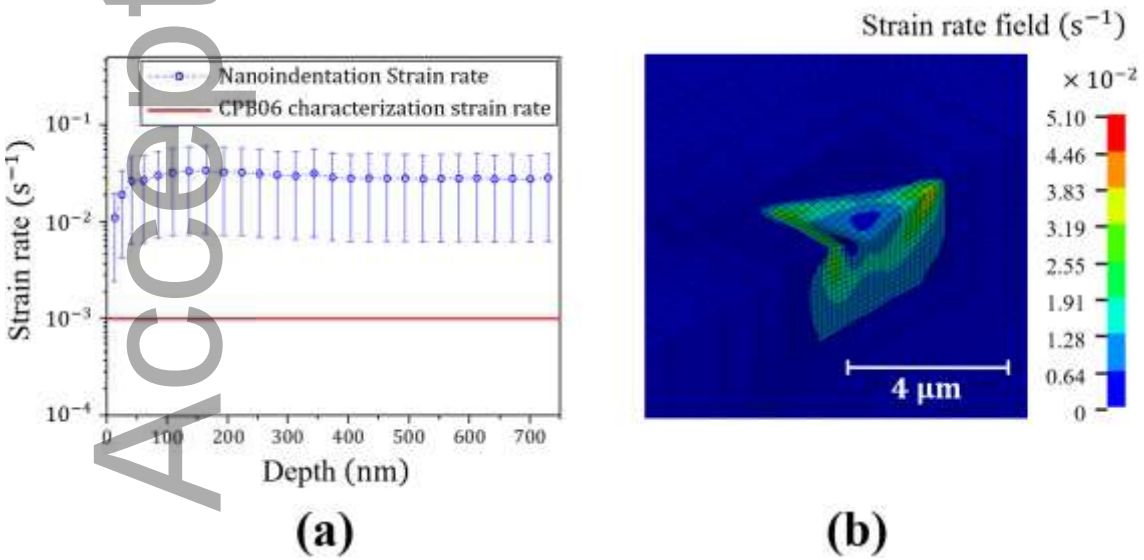

Figure 8. **(a)** Average strain rate in plastic zone of Ti–6Al–4V specimen during nanoindentation simulation and **(b)** strain rate field over Ti–6Al–4V specimen at maximum depth.

Table 1. Experimental elastic modulus of Ti–6Al–4V alloy at a strain rate of 10^{-3} [s^{-1}].

Test	Direction	Young Modulus, E [GPa] / St. Dev.
Tension	LD	111±1
	TD	115±4
	ST	117±1
Compression	LD	122±1
	TD	128±3
	ST	123±3

Table 2. Elastic and elastoplastic orthotropic constants for CPB06 yield criterion for modeling the mechanical behavior of Ti–6Al–4V alloy.

Orthotropic elastic constants						
E_{11}	E_{22}	E_{33}	G_{12}	G_{13}	G_{23}	$\nu_{12}=\nu_{13}=\nu_{23}$
122	128	123	42.629	44.23	45.0	0.30

Components of the orthotropic constants tensor **L**								
Surface	W^P	L_{11}	L_{12}	L_{13}	L_{22}	L_{23}	L_{33}	$L_{44}=L_{55}=L_{66}$
1	1.857	1	-2.373	-2.364	-1.838	1.196	-2.444	-3.607
2	9.377	1	-2.495	-2.928	-2.283	1.284	-2.446	4.015
3	48.66	1	-2.428	-2.920	1.652	-2.236	1.003	-3.996
4	100.2	1	-2.573	-2.875	1.388	-2.385	0.882	-3.926
5	206.6	1	-2.973	-2.927	0.534	-2.963	0.436	-3.883

Table 3. Asymmetry parameters and Voce hardening law (Equation 5) coefficients for (IJP) and (MEC) identifications.

Surface	1	2	3	4	5
k (IJP)	-0.136	-0.136	-0.165	-0.164	-0.180
k (MEC)	-0.136	−0.135	-0.125	-0.114	-0.110

LD Tension (IJP)	R_0=921.0 (MPa)	R_S=160.0 (MPa)	C_R=15.48
LD Tension (MEC)	R_0=918.0 (MPa)	R_s=290.0 (MPa)	C_R=5.80

Table 4. CPB06 effective stress and equivalent plastic strain fields in nanoindentation FE simulation using MEC parameters.

CPB06 effective stress

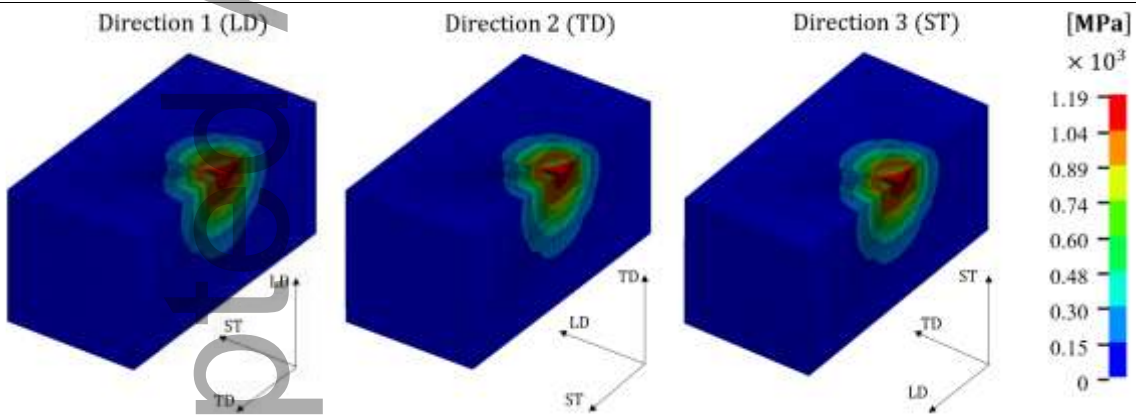

Equivalent plastic strain

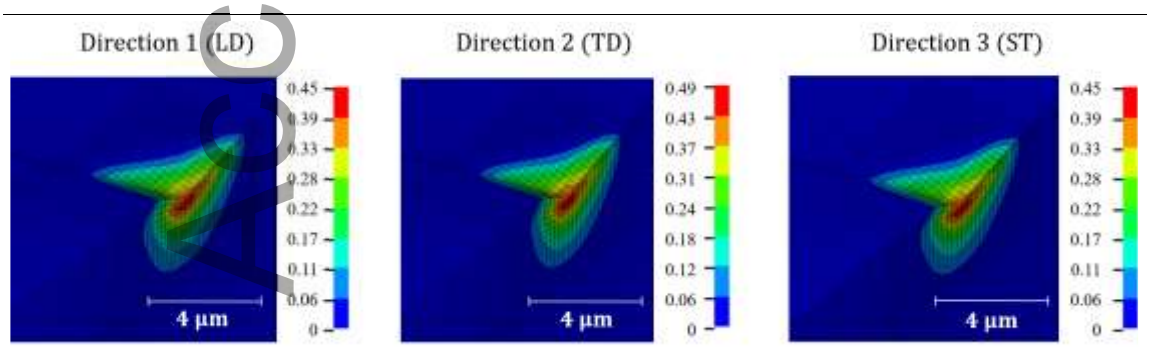

Table 5. P-h curves from three orthogonal nanoindentation simulations.

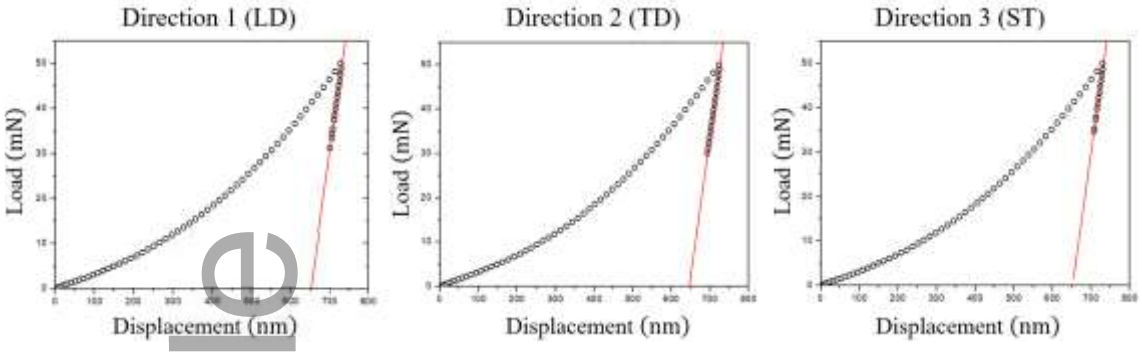

Direction	h_{max} [nm]	S_k [Nm^{-1}]	h_p [nm]	A_{pml} [m^2]
1 (LD)	729.5	6.13×10^{5}	651.1	1.041×10^{-11}
2 (TD)	722.8	6.26×10^{5}	646.2	1.026×10^{-11}
3 (ST)	729.5	6.21×10^{5}	651.6	1.043×10^{-11}

Table 6. Reduced elastic moduli for the three nanoindentation FE simulations following Vlassak & Nix method.

	Reduced Elastic Moduli [GPa] / St. Dev.
Direction 1 (LD)	162.8±4.07
Direction 2 (TD)	167.6±4.20
Direction 3 (ST)	164.8±4.12

Table 7. Experimental and numerically obtained Elastic moduli (GPa) of Ti–6Al–4V, following Oliver & Pharr and Delafargue & Ulm methods.

Direction	Orthotropic elastic moduli of Ti–6Al–4V indented specimen [GPa] / St. Dev.

	Experimental	Oliver & Pharr method	Delafargue & Ulm method
1 (LD)	122±1	148±3.7	117±2.9
2 (TD)	128±3	153±3.8	123±3.1
3 (ST)	123±3	150±3.8	120±3.0

The novel numerical-experimental approach for characterizing orthotropic and asymmetric alloys by combining nanoindentation, scanning electron microscopy and finite element modeling enables accurate and non-destructive testing with reduced amount of sampling material. The validated CPB06 model with enhance capabilities allows predicting elastoplastic deformation response of titanium alloys for biomedical and aerospace applications.

Characterization techniques

C. Rojas-Ulloa, C. Bouffioux, A. Jaramillo, C. M. García-Herrera, T. Hussain, L. Duchêne, G. Riu, J. J. Roa, P. Flores, A. M. Habraken, V. Tuninetti*

Nanomechanical characterization of the deformation response of orthotropic Ti-Al-4V